International Journal of Plasticity 203 (2026) 104724

Contents lists available at ScienceDirect

International Journal of Plasticity

journal homepage: www.elsevier.com/locate/ijplas

Particle-induced void growth under shear loading revealed by 3D X-ray laminography and finite element modeling

Mathias Hurst [a,d,*], Jean-Michel Scherer [b], Xiang Kong [b,c], Maryse Gille [b], Simon Bode [a], Djamel Missoum-Benziane [b], Tilo Baumbach [a,d], Lukas Helfen [a,e], Thilo F. Morgeneyer [b]

[a] Institute for Photon Science and Synchrotron Radiation (IPS), Karlsruhe Institute of Technology (KIT), Eggenstein-Leopoldshafen, Germany
[b] MINES Paris, PSL University, Centre des Matériaux, Versailles, France
[c] Department of Materials, ETH Zürich, Zürich, Switzerland
[d] Laboratory for Applications of Synchrotron Radiation (LAS), Karlsruhe Institute of Technology (KIT), Karlsruhe, Germany
[e] Institut Laue Langevin, Grenoble, France

ARTICLE INFO

Keywords:
Ductile fracture
Shear
Non-proportional loading
Damage growth
Void-locking
Microtomography

ABSTRACT

We present a quantitative, multiscale, four-dimensional study of ductile damage evolution during a "tension-to-shear" load path change in a recrystallized AA2198-T851 alloy sheet. Significant strain and damage develop under tension, and their subsequent evolution under shear is quantified. Damage mechanisms are characterized using synchrotron-based in situ 3D X-ray laminography, complemented by correlative surface imaging. Mesoscale strain fields, measured via projection digital image correlation and validated through simulations, guide the selection of representative regions of interest and their boundary conditions for detailed microscale analysis within the sample bulk. Damage features are either grain-related or intermetallic particle-induced. Grain-related damage shows only moderate evolution under shear, with volume increases of a factor one and a half, whereas intermetallic particle-induced voids exhibit pronounced growth, with volume increases up to factor of six. To elucidate the underlying mechanism, experimentally observed particle–void clusters are investigated using three-dimensional finite element modeling initialized with measured boundary conditions. The simulations reproduce the strong shear-driven void growth via a void-locking mechanism associated with stiff intermetallic particles. In their absence, simulations predict a strongly reduced void growth under shear, confirming the critical role of intermetallic particles in shear-driven damage evolution.

1. Introduction

Stress triaxiality, defined as the ratio of hydrostatic and deviatoric stresses, is a crucial parameter influencing the nucleation and growth of damage in ductile metals. Variation in stress triaxiality causes different strain to fracture (Bao and Wierzbicki, 2004; Papasidero et al., 2015; Roth and Mohr, 2016). While the mechanisms of damage formation under high stress triaxiality are commonly described and understood by nucleation, growth and coalescence (Pineau et al., 2016), underlying mechanisms at low stress triaxiality $\eta < 1$, remain unclear. In particular, no void growth is predicted by standard ductile fracture homogenized models of porous materials under zero triaxiality (Gurson, 1977). *Ad hoc* modifications of these models are hence proposed to

* Corresponding author.
E-mail address: mathias.hurst@kit.edu (M. Hurst).

https://doi.org/10.1016/j.ijplas.2026.104724
Received 25 February 2026; Received in revised form 4 May 2026
Available online 14 May 2026

account for damage under shear (Nahshon and Hutchinson, 2008). Moreover, dependencies between strain to fracture and stress triaxiality are varying (Bao and Wierzbicki, 2004; Papasidero et al., 2015). Furthermore, the impact of non-proportional load paths on strain to fracture, which may exhibit decreased (Kong et al., 2022) or increased fracture strains compared to proportional loading scenarios (Brünig et al., 2021; Wei et al., 2024), is not understood but highly application relevant. *E.g.* during forming and in service conditions the loading path for automotive sheets may completely change.

So far, few studies have investigated the relationship between microstructure and strain for damage formation under low stress triaxiality or non-proportional loading. *In situ* scanning electron microscopy (SEM) studies have observed damage nucleation under shear, where in an AA6061-T6 alloy, nucleation occurred through the cracking of intermetallic particles (Gross and Ravi-Chandar, 2016). Similarly, in high strength low-alloy steels, damage formation under shear involved particle decohesion and void growth around intermetallic particles (Achouri et al., 2013). However, such 2D *in situ* SEM studies are limited by surface effects and a few observed damage features.

For the investigation of fracture mechanisms inside bulk samples, X-ray computed tomography (CT) (Maire and Withers, 2014; Wu et al., 2017), allows for the quantification of damage formation with a statistical relevance inside pin-like specimens. This has been extensively used for *ex situ* and *in situ* studies, providing important information on damage nucleation (Babout et al., 2004; Landron et al., 2010; Toda et al., 2017) and growth (Maire et al., 2011; Landron et al., 2011; Croom et al., 2019; Madi et al., 2019). Moreover, dependencies of fracture on the material's microstructure (Hannard et al., 2016) and the loading direction (Hannard et al., 2018) have been found. Advanced 3D image analysis allowed to track and observe single voids (Lecarme et al., 2014; Azman et al., 2022). However, studies under variable stress states and inside rolling treated materials typically require sheet-like specimens, for which CT is inapplicable. To address these limitations, so-called synchrotron *in situ* X-ray computed laminography (CL) (Helfen et al., 2005; Morgeneyer et al., 2014) can be utilized to study damage mechanisms under shear loading. CL is a generalization of CT, allowing for an inclination of the rotation axis, enabling the 3D investigation of regions of interest inside sheet-like specimens at high resolution. Laminographic observations inside an AA2024-T3 alloy revealed damage nucleation through the fracture or debonding of intermetallic particles, followed by growth of the void volume fraction (Tancogne-Dejean et al., 2021). These effects can be explained qualitatively by the so-called void-locking mechanism (Tvergaard, 2011).

Similarly, for the AA2198-T851 alloy sheet of the present study damage mechanisms under shear loading (Buljac et al., 2023) and non-proportional load path changes from 'shear to tension' (Kong et al., 2022) were investigated by *in situ* laminography. For this material, large damage features, identified as grain-related (Kong et al., 2024), were found to play a crucial role in failure, independent of intermetallic particles. It was found, that grain-related and intermetallic-related damage features nucleate under shear loading and subsequently grow under tension until failure, where the grain-related features turn out to be the detrimental ones. X-ray nanolaminography (Hurst et al., 2023) and electron backscatter diffraction corroborated that these grain-related cracks might occur as intergranular and transgranular cracks (Kong et al., 2024). Such flat cracks can also be observed under tension load (Morgeneyer et al., 2014). An overview on the characterization of ductile fracture mechanisms under low stress triaxiality and non-proportional loading can be found in Han et al. (2024). Despite these advancements, the understanding of damage mechanisms under shear and non-proportional loading, particularly the role of the above-mentioned large flat cracks, remains limited. Additionally, the investigation of flat cracks and intermetallic-related damage and their evolution lacks quantification.

Concerning the micromechanical modeling of damage mechanisms under shear loading, Fleck et al. (1989) and Kuna and Sun (1996) investigated the effect of void nucleation from rigid particles and growth on macroscopic stress–strain behavior under shear and their softening effect in a shear band. They found that accounting for particle-matrix contact was important. Following these results, Siruguet and Leblond (2004) developed an extension of the homogenized Gologanu-Leblond-Devaux (GLD) model (Gologanu et al., 1997) to account for the influence of inclusions on void growth at low ($\lesssim$0.77) stress triaxiality. Tvergaard (Tvergaard, 2008, 2009) simulated the behavior of voids under simple shear in 2D and found void rotation and elongation. This process leads to final closure of voids and also to macroscopic localization. A 3D simulation for spherical voids has been carried out in (Nielsen et al., 2012). Torki and Benzerga (2018) investigated the process of void-mediated failure inside a naturally forming, i.e. stress triaxiality larger than zero, shear band and carried out numerical simulations using a continuum micromechanics framework for dilatant plasticity that captured the essential features of sub-cell deformation: a. void-induced strain localization; b. void rotation; c. void elongation.

This study investigates damage mechanisms in an AA2198-T851 alloy sheet under a tension-to-shear (TS) load-path change, aiming at the understanding of particle-related damage mechanisms. The load-path change introduces significant damage during the tensile phase, enabling observation and quantification of damage growth, during the subsequent shear loading. The present work investigates specifically particle-induced damage growth under shear, thereby complementing existing nano- and microscale investigations of shear-induced damage mechanisms (Kong et al., 2022, 2024; Han et al., 2024). To acces the dynamics of microscale particle-related damage a multiscale analysis is conducted. Macro- and subsequent mesoscale characterization provide access to grain-scale damage and strain fields, which are used to identify regions of interest for detailed microscale investigation. On the microscale, damage mechanisms arising from interactions between intermetallic particles and voids are quantified. Morphological damage evolution is measured using CL and validated using 3D finite element modeling (FEM), by careful extracting the boundary conditions from the mesoscale strain fields and meshing the digital twin of a particle-void cluster formed during the tension stage.

Characterization techniques include synchrotron *in situ* X-ray laminography for the microstructure and strain evolution measurements on the meso- and microscale. Additionally, correlative surface microscopy (Hurst, 2024) enables macroscopic extensometer, displacement, and strain measurements at the sample's surface based on digital image correlation (DIC). To validate measured mesoscale deformation existing elasto-plastic models (Kong et al., 2023) are employed. To access stress triaxiality of the material's behavior and model the evolution of particle related damage 3D FEM (Besson and Foerch, 1997) are employed on the meso- and microscale.

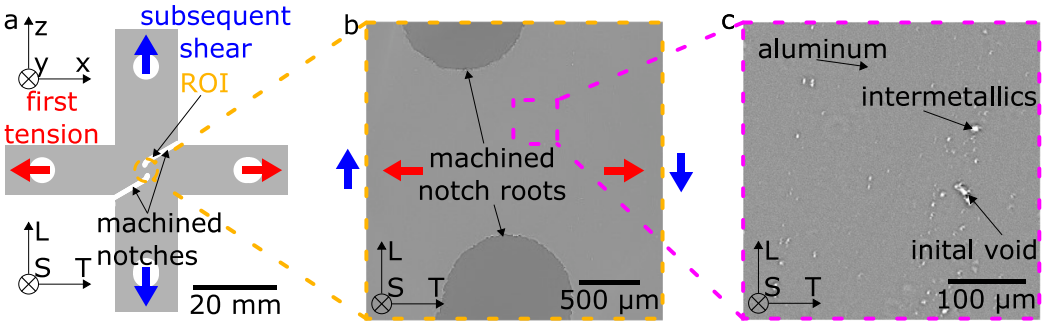

Fig. 1. Description of the material and 'tension to shear' specimen geometry. (a) full specimen geometry and coordinate systems. The material's coordinate system is represented by TSL, while the global coordinate system is denoted by xyz. The investigated ROI and loading directions for shear and tension are indicated. (b) a 2D slice of reconstructed 3D laminography data displaying the acquired ROI, illustrating the sample geometry and loading directions for shear and tension. (c) zoomed-in region of the ROI to show the material's microstructure, containing three phases: aluminum matrix (gray), intermetallic particles (white) and initial voids (black).

2. Material & experimental methods

2.1. Material

The investigated material is a recrystallized AA2198-T851 aluminum (Al-Li-Cu) alloy, widely used in aircraft applications due to its outstanding mechanical properties and low density. The investigated material is provided by *Constellium Technology Center (C-TEC), Voreppe, France* and was heat treated under T851 conditions. The microstructure of the material in its undeformed state is shown in Fig. 1(c), comprising three phases: the aluminum matrix (gray), intermetallic particles (white) with a volume fraction of approximately 0.3 % to 0.4 % (Morgeneyer et al., 2014), and initial porosity (black) with a volume fraction of ≤0.03 % (Morgeneyer et al., 2014). The TSL coordinate system, illustrated in Fig. 1, denotes the material's processing directions: L for the rolling direction, *T* for the transverse direction, and S for the short transverse direction. The alloy's average grain size, measured by electron backscatter diffraction, is $82 \times 80 \times 20\,\mu m^3$ (Kong et al., 2022). The material's composition (wt%) is as follows: 2.9–3.5 Cu, 0.8–1.1 Li, 0.25–0.8 Mg, 0.1–0.5 Ag, 0.04–0.18 Zr (Morgeneyer et al., 2014).

2.2. Mechanical testing

The specimen geometry for the tensile experiment is identical to the specimen investigated in 'shear to tension' load path change experiment (Kong et al., 2022) and is inspired by Roth and Mohr (2018). As depicted in Fig. 1, the cruciform shape enables both shear and tension loading of the region of interest (ROI), marked in Fig. 1(a), facilitated by specific machined notches, indicated in Fig. 1(a) and (b). This geometry has been revised and optimized through FEM, with the size of the ROI adjusted to align with the available field of view (FOV) of X-ray computed laminography (CL). The specimen, with a nominal thickness of 1 mm, was produced via electrical discharge machining. To delineate the loading directions, we introduce an experimental coordinate system xyz, depicted in Fig. 1 which, in the undeformed state, aligns with the TSL coordinate system. Tension stress is applied by loading along the x direction, while shear stress is applied, by loading along the z direction after rotating the sample in the loading frame. The resulting deformation is described by the deformation gradient, **F**, which is composed by a rotation matrix **R**, describing a rigid body motion and the symmetric stretch tensor (for reference see Kong et al. (2022)):

$$\mathbf{U} = \begin{bmatrix} U_{xx} & U_{zx} \\ U_{zx} & U_{zz} \end{bmatrix}. \tag{1}$$

Where U_{xx} denotes the tension stretch, and U_{zx} the shear stretch applied during the TS experiment.

For mechanical loading, we utilized a dedicated tensile machine designed specifically for *in situ* synchrotron laminography measurements (see Fig. 2(b) and (c)). The loading experiment was displacement controlled. Although the loading machine allows only uniaxial loading, a simple unloading and rotation of the cruciform sample permits for biaxial load path changes, as illustrated in Fig. 2(c). For the 'tension to shear' (TS) load path change (LPC) presented here, the sample was incrementally loaded to enable 3D measurements of the sample's microstructure and the measurement of the sample's macroscopic deformation at the surface (for measurement details, see Sections 2.5 and 2.6). In total, the sample underwent 22 incremental loading steps until failure. Tension loading was applied for load steps 1–9 up to a tension pre-stretch of $U_{xx} = 1.09$, while for load steps 10–22 the specimen underwent shear loading up to a stretch of $U_{zx} = 0.15$. The relatively high tension pre-stretch was chosen to initiate damage, the behavior of which could then be studied under shear. The resulting load curves for the tension phase of the LPC experiment are shown in Fig. 3 (d, red), and for the shear phase in Fig. 3 (e, blue), compared to monotonic tension-only and shear-only experiments, as well as the simulation of the TS LPC. Further discussion and precise descriptions are provided in Section 3. Multiple experiments have been conducted on identical specimens (Kong et al., 2023), revealing ductility scattering of $U_{xx} = 1.106 - 1.130$ for monotonic tension-only loading, $U_{zx} = 0.132 - 0.137$ for monotonic shear-only loading, and $U_{zx} = 0.118 - 0.158$ for biaxial tension-shear loading. The ductility scatter is indicated in Fig. 3(d) and (e).

2.3. Continuum scale modeling of the material

To predict accumulated equivalent strain (acc. eq. strain) and stress triaxiality during the TS LPC conducted in this study, the finite element software Z-set (Besson and Foerch, 1997) was employed, following the procedure proposed in Kong et al. (2023, 2022). An elasto-plastic material law accounting for the plastic anisotropy of the material was used. The model is based on the anisotropic yield function proposed in Bron and Besson (2004). Strain hardening is modeled with a two-exponential isotropic hardening function. The model parameters and their identification procedure are based on various mechanical tests in different material directions, which can be found in Kong et al. (2023). The simulations steps involved are as follows: (i) The material orientation in simulations is initialized so that the transverse direction T is aligned with the tensile direction x and the rolling direction L is aligned with the shear direction z (see Fig. 1). (ii) To reduce computational effort, only half of the specimen thickness was modeled using quadratic tetrahedral elements, owing to the symmetric geometry. Otherwise, the modeled specimen geometry corresponds to the experimental specimen. (iii) The element size of the mesh varied from 30 µm to 100 µm. A visualization of the full mesh can be found in Kong et al. (2022). (iv) A mixed displacement-pressure updated Lagrangian formulation was applied for the tetraedral element (c3d10) to account for large plastic strain and incompressibility. (v) To simulate loading, steel pins were modeled at the foreseen holes (see Fig. 1). (vi) The tension stretch U_{xx} and shear stretch U_{zx} measured by correlative surface microscopy and evaluated by the 4 point extensometer (see Fig. 3(a) and (b)) were applied using a strain rate of 10^{-4} s^{-1}. (vii) The displacement values measured from correlative surface microscopy and DIC were used to relate to the FEM simulation, as illustrated in Fig. 3(c). (viii) Stress triaxiality η is defined as the ratio of the mean stress σ_m to the equivalent stress σ_{eq}.

Resulting surface displacements, internal triaxialities, and internal strains are presented in Figs. 3(c), 4, 5–7, and 8, and are analyzed and discussed further in the results and discussion section. Due to the chosen mesh parameters and the resulting deformations, a simulation up to load step 19 was feasible.

2.4. Micromechanical modeling accounting for particles and voids

To understand the role of particles in the observed growth of voids under shear loading, micromechanical simulations of particle-void clusters were performed. The pre-tension phase is not modeled in these simulations, but particles with pre-existing cracks are considered as the initial condition. Two geometries are considered (see Fig. 12): (i) a simplified particle-void cluster consisting of a single ellipsoidal particle with a 45° slanted initial crack and (ii) a digital twin of a measured particle-void cluster.

The same elasto-plastic material law as in the continuum scale modeling was used for the aluminum matrix surrounding the particle-void cluster. The particles (red in Fig. 12) are considered isotropic elastic with a Young's modulus of 235 GPa and a Poisson's ratio of 0.3 (Zhang et al., 2021). To understand the role of particles on void growth under shear loading, the same crack geometries (blue Fig. 12) were also considered without their surrounding elastic particle. These configurations are denoted as 'no particle' in Fig. 12. A mixed displacement-pressure updated Lagrangian formulation was applied for the tetraedral element (c3d10_4) to account for large plastic strain and incompressibility. The element size varies from 0.5 µm to 3 µm in the simplified particle-void cluster and from 1 µm to 6 µm in the measured particle-void cluster

Two kinds of boundary conditions (BC) are considered: (i) displacements extracted from a square region of interest in the DIC field where the particle-void cluster is located as marked with a red cross in Figs. 5 and 6 (denoted as 'measured BC' in Fig. 12) and (ii) simplified DIC-measured displacements, where the x-component of the displacement was dropped to keep only the dominant shear component along z (denoted as 'idealized BC' in Fig. 12). This idealized BC corresponds to simple shear. It is considered in order to remove any potential parasitic tensile component which could stem from DIC errors and focus only on the shear loading component. The resulting average stretch components and void volume evolution are post-processed and plotted against the accumulated equivalent strain in Fig. 12.

2.5. Macroscale characterization methods

Macroscopic deformation at the sample surface is measured by means of *in situ* surface microscopy (Hurst, 2024). Therefore, a suitable, retractable visible light microscopy setup is integrated within the laminography station above the loading device (see Fig. 3). The microscopy setup consists of a Basler acA2040-25gm camera (*Basler AG, Ahrensburg, Germany*) coupled to a Mitutoyo VMU-V microscope and a Mitutoyo M Plan Apo 2x objective lens, (both *Mitutoyo Deutschland GmbH, Neuss, Germany*). This setup provides an effective pixel size of 2.75 µm and a field-of-view (FOV) of $5.6 \times 5.6\,mm^2$. To facilitate deformation measurement, the sample surface is prepared with a speckle pattern. The surface is colored directly before the experiment in order to ensure ductile behavior, the resulting speckle pattern is shown in Fig. 3(a). From the surface images, acquired *in situ* during the loading experiment displacement fields D_z are determined using digital image correlation (DIC). For DIC analysis the software VIC-2D 7 (*Correlated Solutions, Irmo, USA*) has been employed using a subset size of 261 µm. The macroscopic stretch matrix **U** (see Section 2.2) is measured by a four point extensometer, depicted for a selected load step in Fig. 3(a) and (b), with an initial size of $0.9 \times 1.6\,mm^2$. The resulting stress stretch curves can be found in Fig. 3(d) and (e). Where stress is defined as (F/S_0) with the force F and S_0 being the initial cross-section of the investigated ROI before loading.

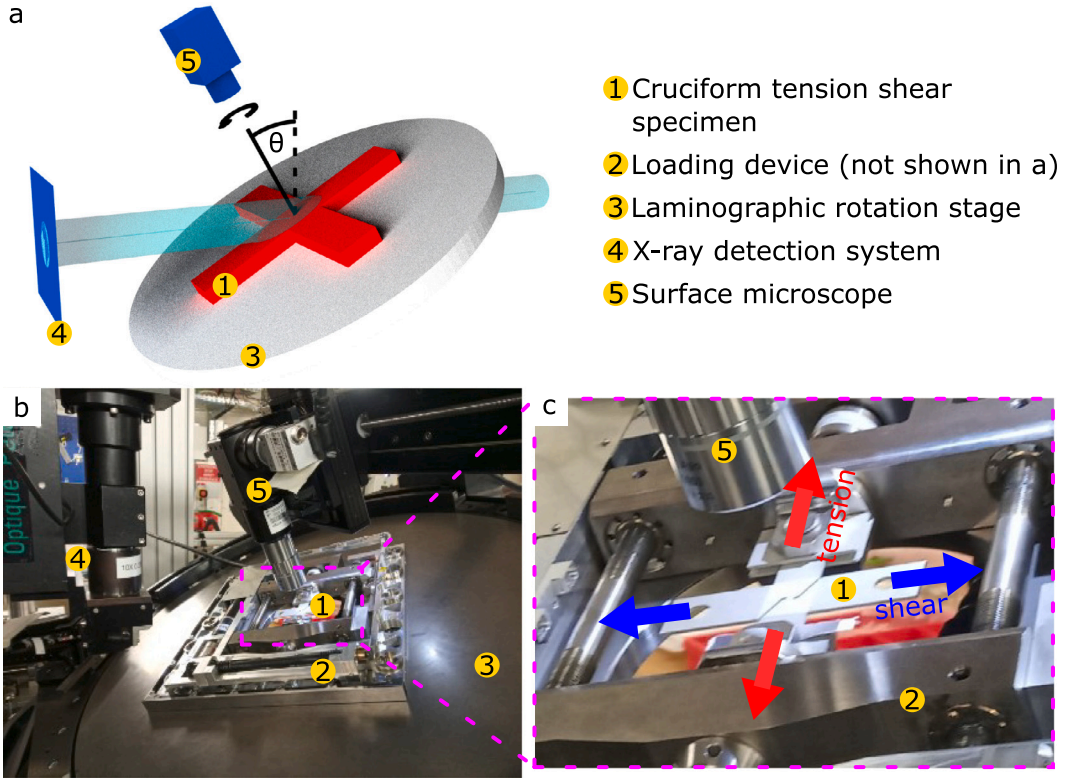

Fig. 2. *In situ* X-ray laminography, implemented at beam line ID19 of the ESRF. (a) illustration of the laminographic measurement principle, with the rotation axis inclined by the laminographic angle θ. The setup includes an X-ray detector and a visible light surface microscope. (b) photograph of the actual setup, featuring the tensile loading machine. (c) zoomed view of the cruciform sample mounted in the loading machine. To switch between tension and shear loading, the sample is unloaded and subsequently rotated by 90° inside the loading machine.

2.6. Meso- and microscale characterization methods

Meso- and microscale studies, presented in this work, are based on synchrotron computed laminography (CL) (Helfen et al., 2005). CL generalizes computed tomography, allowing for a tilt of the rotation axis out of the beam normal, enabling the imaging of the 3D microstructure in regions of interest inside flat, and laterally extended specimens without sample dissection (an illustration of the CL measurement geometry can be found in Fig. 2(a)).

Micro- and mesoscale fracture kinetics were measured by *in situ* CL. The experiment was performed at ESRF ID19 using an experimental setup dedicated for CL (see Fig. 2(b)). The laminographic angle was adjusted to $\theta = 26.2°$, and 3600 projections were acquired with an exposure time of 0.19 s. For correction of the beam profile and detector noise characteristics, 50 flat-field images and 50 dark-field images were acquired. X-ray radiation from an undulator source with a peak energy of 26 keV was employed. For detection an indirect detector system from *Optique Peter, Lentilly, France*, equipped with a 25 µm LuAG scintillator and a 7.5x M Plan Apo objective (*Mitutoyo Deutschland GmbH, Neuss, Germany*), was used. The magnified image was recorded with a PCO.Edge 5.5 camera (*PCO, Kelheim, Germany*). This configuration provided an effective voxel size of 0.96 µm and a FOV of $2.56 \times 2.56 \times 2$ mm.

The *in situ* loading device and the optical microscope for surface observation were integrated into the CL setup (see Fig. 2), enabling the loading process as well as data acquisition to be performed *in situ*.

In total, 22 laminographic scans were acquired: scans 1–9 involved tension loading, while scans 10–22 involved shear loading.

An additional laminographic scan of the specimen was acquired after fracture to gain insight into the fracture path. The measurement was performed at an experimental CL setup located at the IMAGE beam line of KIT Light source (Cecilia et al., 2025) employing filtered white-beam originating from a wiggler source. The laminographic angle was adjusted to $\theta = 30°$ and 4000 projections, 100 dark-field images, and 100 flat-field images were acquired with an exposure time of 0.2 s. For detection an indirect detector system from *Optique Peter, Lentilly, France*, equipped with a 13 µm LSO scintillator and a 7.5x M Plan Apo objective (*Mitutoyo Deutschland GmbH, Neuss, Germany*), was used. The magnified image was recorded with a PCO.Edge 5.5 camera (*PCO, Kelheim, Germany*), resulting in an effective voxel size of 0.96 µm.

Prior to 3D reconstruction by filtered backprojection (Myagotin et al., 2013) using the tofu framework (Faragó et al., 2022), flat- and dark-field correction was performed. The *in situ* data was registered and a ROI, containing the strained region of the sample ($1.44 \times 1.92 \times 0.38$ mm^3) was selected.

The fracture path was extracted from the *ex situ* measurement by averaging several slices and applying a Sobel filter for edge detection (Kanopoulos et al., 1988).

To extract morphological measures of the damage evolution, the laminographic data was segmented. Segmentation of mesoscale features was performed using a combination of threshold segmentation of grayscale values and cluster sizes. The cluster size threshold precludes the influence of noise and laminographic artifacts.

The grayscale threshold was selected with respect to the histogram of the 3D laminographic volumes. The cluster size threshold was adjusted to 88.1 μm^3, corresponding, for example, to a cluster with a size of $4.45 \times 4.45 \times 4.45\ \mu m^3$. As a result, smaller voids are not taken into account, in particular, this refers to intermetallic-related damage.

The segmentation of the microscale features, like intermetallic-related damage, was performed manually. Segmentation and quantification was performed using a Python-based in-house software.

To measure strain within the sample, so-called projection DIC (P-DIC) (Kong et al., 2022; Morgeneyer et al., 2021; Gille et al., 2024) was employed. Therefore, the central 100 slices (96 µm) of the specimen were selected and projected along the y-direction using a maximum norm. The resulting images were subsequently correlated by means of DIC. The analysis was performed using VIC-2D 7 (*Correlated Solutions, Irmo, USA*) with a subset size of 91 µm. In comparison to digital volume correlation, P-DIC allows extracting 2D internal strain fields even for low marker densities. It assumes that strain along the projection direction is negligible, which applies well to the 2D specimens presented here. Resulting strains are expressed by the accumulated equivalent (acc. eq.) Hencky strain Roth and Mohr (2016), Tancogne-Dejean et al. (2021) and Kong et al. (2022), allowing for a cumulative quantification of strain during the load path change experiment. According to Abedini et al. (2018), acc. eq. strain is calculated by

$$\Delta\varepsilon_{\mathrm{eq}} = \frac{2}{\sqrt{3}}\sqrt{\Delta\varepsilon_{\mathrm{I}}^2 + \Delta\varepsilon_{\mathrm{I}}\Delta\varepsilon_{\mathrm{II}} + \Delta\varepsilon_{\mathrm{II}}^2} \tag{2}$$

using the increment of the principal logarithmic strain components $\Delta\varepsilon_{\mathrm{I}}$ and $\Delta\varepsilon_{\mathrm{II}}$ and the assumption of incompressiblity.

3. Results

3.1. Macroscale observations

Macroscopically, the *in situ* TS LPC is characterized by a 4 point optical extensometer (for details, see Section 2.5). This approach allows for the measurement of tension stretch (U_{xx}) and shear stretch (U_{zx}). The resulting nominal stress–stretch curve for the tension loading is shown in Fig. 3(d), while the stress–stretch curve for the shear part can be found in Fig. 3(e). Both curves are compared to stress–stretch curves of a simulated LPC experiment. Furthermore, the LPC tension phase is compared to a measured stress–strain curve of a monotonic tension-only (TO) experiment, and the LPC shear phase is compared to a measured stress–strain curve for a monotonic shear-only (SO) experiment.

During the tension phase, TS experiment, TS simulation, and TO experiment show good agreement (see Fig. 3(d)). The maximum stresses found are: $(F/S_0)_{\mathrm{LPC,\ tension,\ exp}} = 508$ MPa for the TS experiment, $(F/S_0)_{\mathrm{LPC,\ tension,\ sim}} = 524$ MPa for the simulated TS experiment, and $(F/S_0)_{\mathrm{TO,\ exp}} = 513$ MPa for the TO experiment. The small deviation between simulated and measured TS LPC experiments (for load steps 4–6) can be explained by relaxation, which occurs during the incremental loading (interrupted to perform laminographic scans) of the measurement. Further information on relaxation effects during stepwise loading of AA2198-T8R can be found in Ren et al. (2019). For the simulation, monotonic loading was applied to the specimen. The applied maximum tension stretches are $U_{\mathrm{xx,\ LPC,\ tension,\ exp}} = 1.090$ for the tension phase of the LPC experiment and $U_{\mathrm{xx,\ TO,\ fracture}} = 1.113$ for the TO experiment, where the proportional loading TO experiment involved loading until failure. Several repetitions of the TO experiment (Kong et al., 2023) showed a ductility scatter of $U_{\mathrm{zx,\ TO,\ exp}} = 1.106 - 1.130$. Thus, during the tension phase of the LPC experiment, the specimen was loaded up approximately 96.4 % to 98.5 % of its stretch to fracture. This high pre-stretch was applied with the intention of creating relevant damage at the microscale, the development of which can be studied during shear.

The subsequent shear phase showed good agreement between measured and simulated LPC experiments, but compared to the SO experiment, the LPC experiment exhibited substantially lower maximum stress values and an increased stretch to fracture (see Fig. 3), which is consistent with the net section reduction during the tension phase. The shear stretch offset of the LPC experiment is due to the shear stretch that is generated during the tension part, due to the slight offset of the notches (This offset is needed for the shear part of the experiment to limit failure from the notches). To understand the increased stretch to fracture of the LPC experiment compared to the SO experiment, accumulated local equivalent strain can be considered. Kong et al. (2023) showed by FE simulations that local accumulated equivalent strain is similar for comparable shear stretches during LPC and SO experiments for the studied material. The measured maximum stress values are $(F/S_0)_{\mathrm{LPC,\ shear,\ exp}} = 270$ MPa for the LPC measurement, $(F/S_0)_{\mathrm{LPC,\ shear,\ sim}} = 273$ MPa for the LPC simulation, and $(F/S_0)_{\mathrm{SO,\ exp}} = 321$ MPa for the SO experiment. The measured stretch to fracture values are $U_{\mathrm{zx,\ LPC,\ shear,\ exp,\ fracture}} = 0.154$ for the LPC experiment and $U_{\mathrm{zx,\ SO,\ exp,\ fracture}} = 0.125$ for the SO experiment. With the chosen mesh parameters (for details, see Section 2.3), modeling was only possible until a shear stretch of $U_{\mathrm{zx,\ LPC,\ shear,\ sim}} = 0.121$, corresponding to load step 19/22. This is caused by convergence problems due to highly distorted elements. Like for the TO experiment, during shear ductility scatter is found (Kong et al., 2023). The scatter is $U_{\mathrm{zx,\ LPC,\ shear,\ fracture}} = 0.118 - 0.158$ for the LPC experiment and $U_{\mathrm{zx,\ SO,\ fracture}} = 0.132 - 0.137$ for the SO experiment.

The main observations of the TS LPC experiment on a macroscopic scale are as follows:

- Tension phase: TO, measured LPC, and simulated LPC are in good agreement.
- Shear phase: the current experiment shows increased stretch to fracture of LPC compared to SO and decreased maximum stress for LPC compared to SO. Measured and simulated LPC are in good agreement. The ductility scatter is larger for LPC compared to SO (Kong et al., 2023).

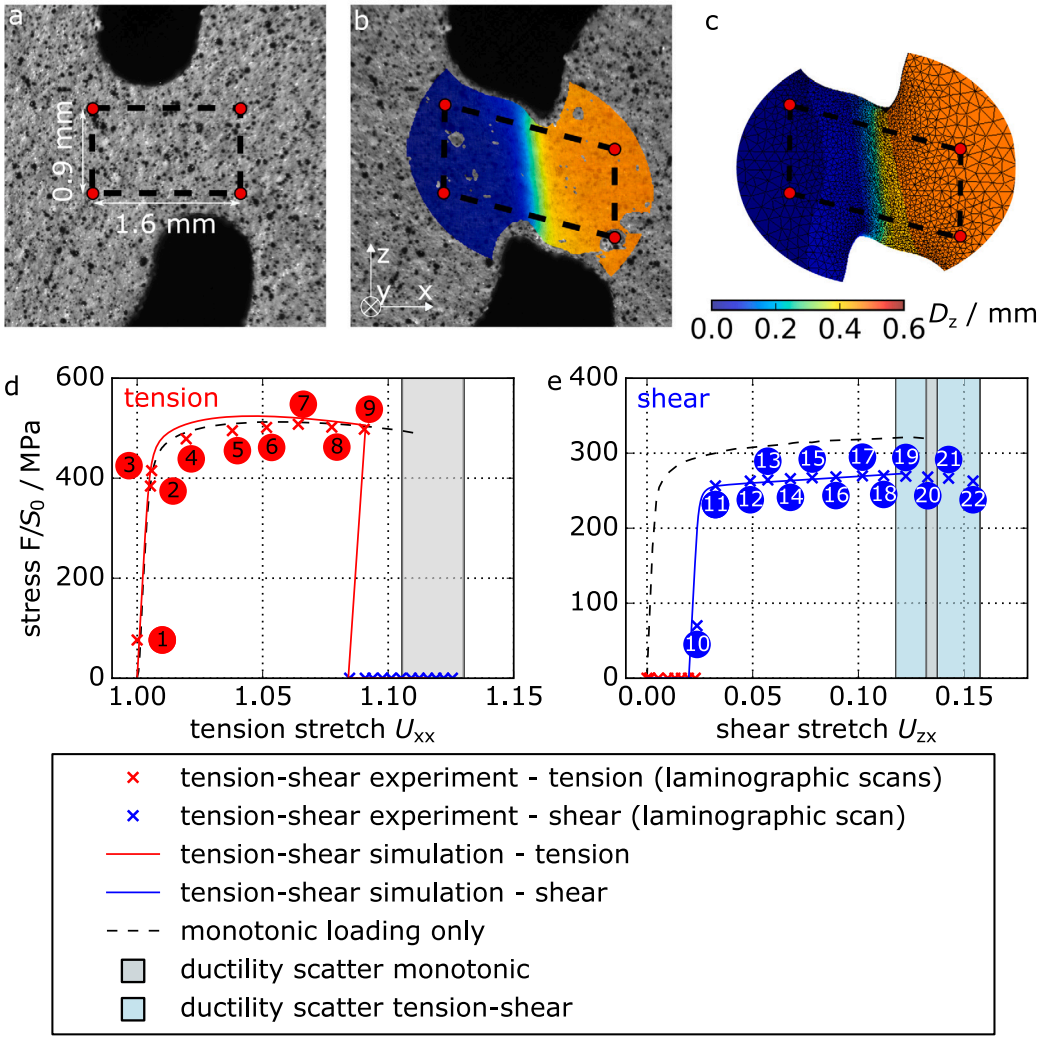

Fig. 3. Macroscale analysis of the *in situ* tensile test and simulation. (a) and (b) images of the sample surface in the undeformed and deformed states (load step 1 and 18). Correlative surface microscopy enables the measurement of the displacement field D_z via DIC and macroscopic deformation using a 4 point extensometer. (c) FEM simulated strain field at load step 18. The FEM simulation is synchronized with the 4 point extensometer measurement. (d) and (e) results of the measured and simulated stress stretch curves of the discussed 'tension to shear' LPC. The data is compared to the results of monotonic tension-only and shear-only experiments.

3.2. Mesoscale observations

Mesoscale processes observed during the LPC experiment mainly involve the nucleation and evolution of larger damage features and strain fields. For selected load steps, the strain damage interaction is depicted in Fig. 5 (tension phase) and Figs. 6 and 7 (shear phase). In the left image, the measured acc. eq. strain and the corresponding simulated acc. eq. strain map (central image) are depicted. The definition of acc. eq. Hencky strain, can be found in Eq. (2). The right image shows the segmented damage field and the notch surface from different view directions. Corresponding images for all load steps can be found in the supplemental information.

During the tension phase, strain is localized mainly at the roots of the machined notches, as shown in Fig. 5. This is particularly visible for load step 9. The maximum measured strain in tension is $\epsilon_{eq,max} = 0.4$. From Fig. 4 it can be concluded, that in the region of strain accumulation the stress triaxiality is close to 1 during the tension phase. Under the subsequent shear load, a shear band with a width of approximately 270 µm forms, as visible in Figs. 6 and 7. The shear band contains localized sub bands, in which the accumulated equivalent strain has maxima. The sub shear bands are mainly elongated in the z direction. This can be observed in Figs. 6–8. In particular, the sub band becomes visible in Fig. 8(c), where a line profile along the strain at the sample's center is shown for different load steps. The line profile shows clearly two maxima. The absolute value of the maxima differs, indicating

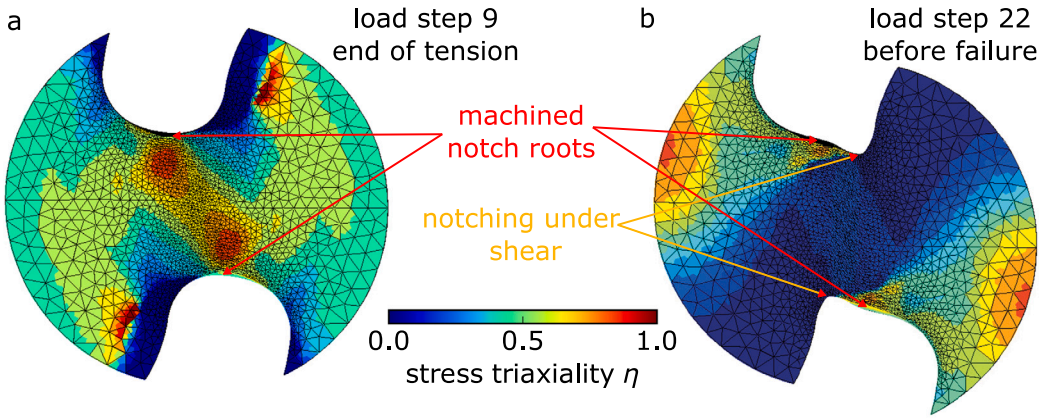

Fig. 4. Simulated stress triaxialities in the central plane: (a) at maximum tension loading, high stress triaxiality is evident at the machined notch roots. (b) during shear loading/before fracture, additional notching with zero stress triaxiality is observed. Sharp stress triaxiality peaks are found at the machined notch root.

differently pronounced sub shear bands. This strain localization in two sub bands is apparent within the whole shear band (all line profiles indicated in Fig. 8(a) and (b) can be found in the appendix). The maximum observed strain before failure is $\varepsilon_{eq,max} = 1.2$. Simulated acc. eq. strain maps are shown in Figs. 5–8. The localization of strain under tension within the machined notch roots is predicted correctly by the employed numerical model. The width of the shear band and its average strain magnitude show good agreement with the measurements. Also, the strongly localized strain peaks in the machined notch root are found in simulated and measured strain fields. However, the observed sub shear bands are not captured by the simulation, as becomes most clear from Fig. 8(c). The stress triaxiality within the shear band is zero (see Fig. 4(b)), but within the machined notch roots (see Figs. 4 and 6), a small, strongly localized region with non-zero stress triaxiality is found.

In the following, the nucleation and development of mesoscale damage features will be quantified and correlated with the strain development described above. For the analysis of mesoscale damage features, only voids/cracks with sizes of $(4.45\,\mu m)^3$ are taken into account according to the cluster size threshold, discussed in Section 2.6. The development of the damage field (blue) and the sample surface (gray) are shown for selected load steps in Figs. 5–7. All load steps are shown in the supplements. As mentioned in Section 2.1, initial damage/porosity in the undeformed state of the material can be neglected. First damage features occur at load step 6 (see Fig. 5) under tension load, and many further damage features nucleate until the end of the tension phase up to load step 9. The damage features nucleated under tension have sizes of a few tens of micrometers up to a few hundreds of micrometers. These damage features accumulate in the regions close to the machined notch root, where strain is localized during tension loading (see Fig. 5). As shown in Fig. 4, in the region where damage nucleates, the stress triaxiality is maximal and close to 1.

The growth of larger damage features (feature volume $\geq (4.45\,\mu m)^3$) can be observed qualitatively in Figs. 5–7 and is quantified in Fig. 9. These features are flat cracks, mainly extended in the z direction. Taking into account the material's grain size and shape, in Kong et al. (2022), we concluded that this type of damage is related to the material's grain structure. Thus, in the following, these large damage features will be denoted as grain-related damage features.

The first grain-related damage features nucleate at load step 5 under tension, followed by a rapid exponential growth in the number of damage features, void volume, and damage surface fraction (Fig. 9(a)–(c)) between load step 5 and load step 8 (corresponding to a max. acc. eq. strain $\varepsilon_{eq} \sim 0.18 - 0.36$). During the tension phase, the number of grain-related damage features rises to 345, and the corresponding surface fraction of projected damage increases to 5.38 %. The damage surface fraction is obtained by projecting the segmented damage field along the x direction (Fig. 9(d)). The observed damage formation during the tension phase is spatially localized at the machined sample notches, where strain is maximum (Fig. 5, load step 9).

During shear, only moderate linear growth of grain-related damage is observed (Fig. 9, load step 10–22, with max. acc. eq. strain $\varepsilon_{eq} \geq 0.44$). Before failure, 527 damage features have been detected, and the total volume of grain-related damage features increased by 45 % during shear loading. The damage surface before fracture was measured to be 6.58 %. The damage nucleation rate (see Fig. 9(a)) shows moderate increase with linear behavior under shear. It should be noted that this value might be influenced by the growth of intermetallic-related damage, which now might exceed the cluster size threshold and contribute, too. Such resolution effects have been found to be uncritical for the quantification of damage growth (Landron et al., 2012), the growth of intermetallic-related damage is further described in Section 3.3.

Additionally, during the shear phase, the formation of sub notches within the machined notch root is observed (Fig. 6). These notches are located at the flank of the specimen's actual machined notch root, where strain with non-zero stress triaxiality is observed during the shear phase (Fig. 4(b)). Moreover, shear notches appear (Fig. 7, load step 20), forming under nearly zero stress triaxiality (Fig. 4(b)).

To contextualize the role of different mesoscale damage features (grain-related tension damage features, high stress triaxiality sub notches in the machined notch root, and shear notches) in the specimen's failure, a post-mortem CL measurement was performed.

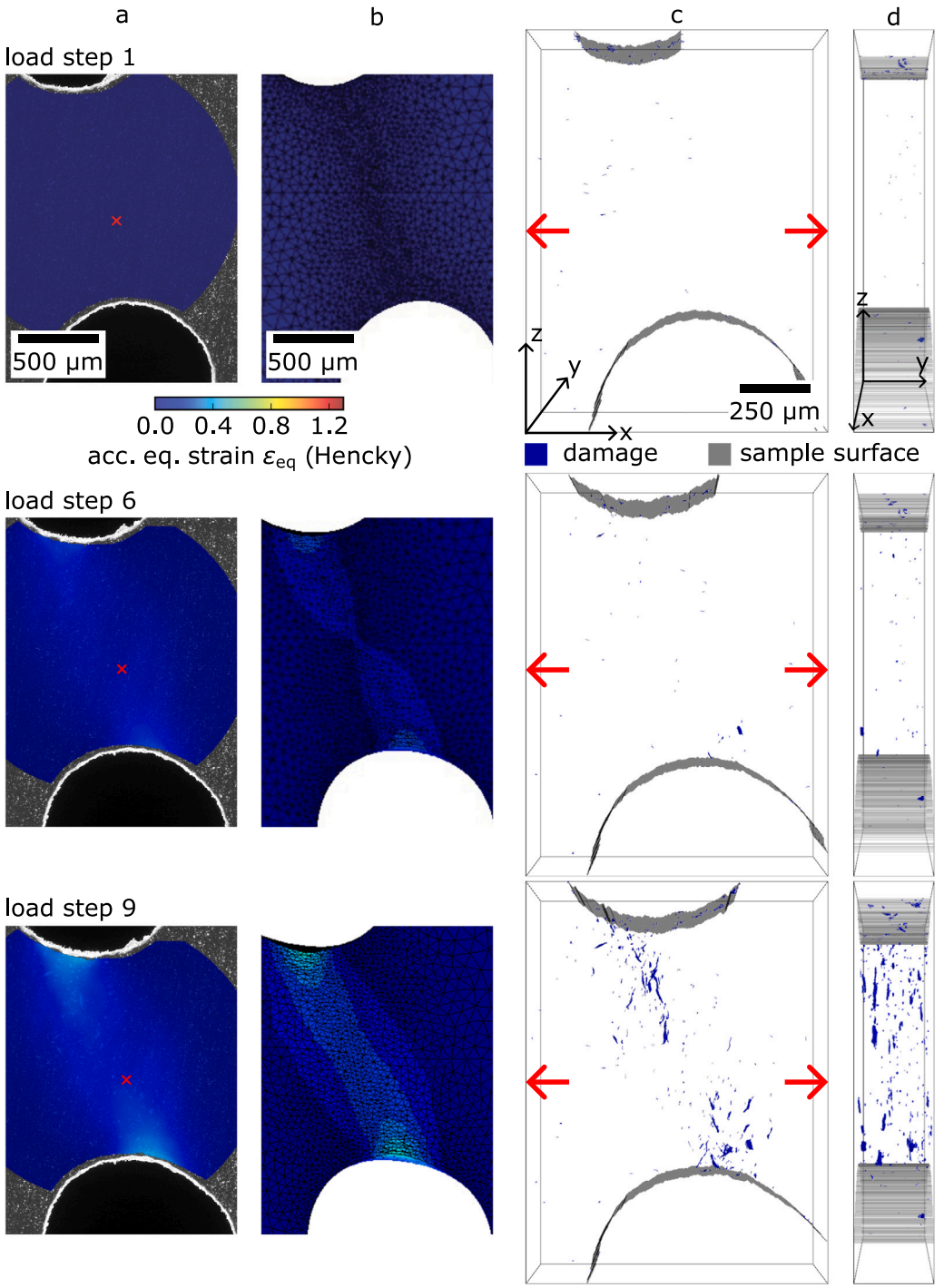

Fig. 5. Mesoscale developments during tension loading. (a) measured and (b) simulated acc. eq. Hencky strain in the sample center. 3D renderings of the corresponding damage features (c) normal to the sheet plane, (d) normal to the fracture plane.

The resulting fracture surface (Fig. 7, load step 22 and Fig. 10(a)), reveals that the specimen fractures from a sub notch in the machined notch root (tension notch) to a shear notch.

Notably, the fracture path coincides with a large, probably grain-related flat crack, further denoted as detrimental damage feature. It is marked in Fig. 10(a), and its detailed development is shown in Fig. 10(b). The detrimental damage feature nucleates at load

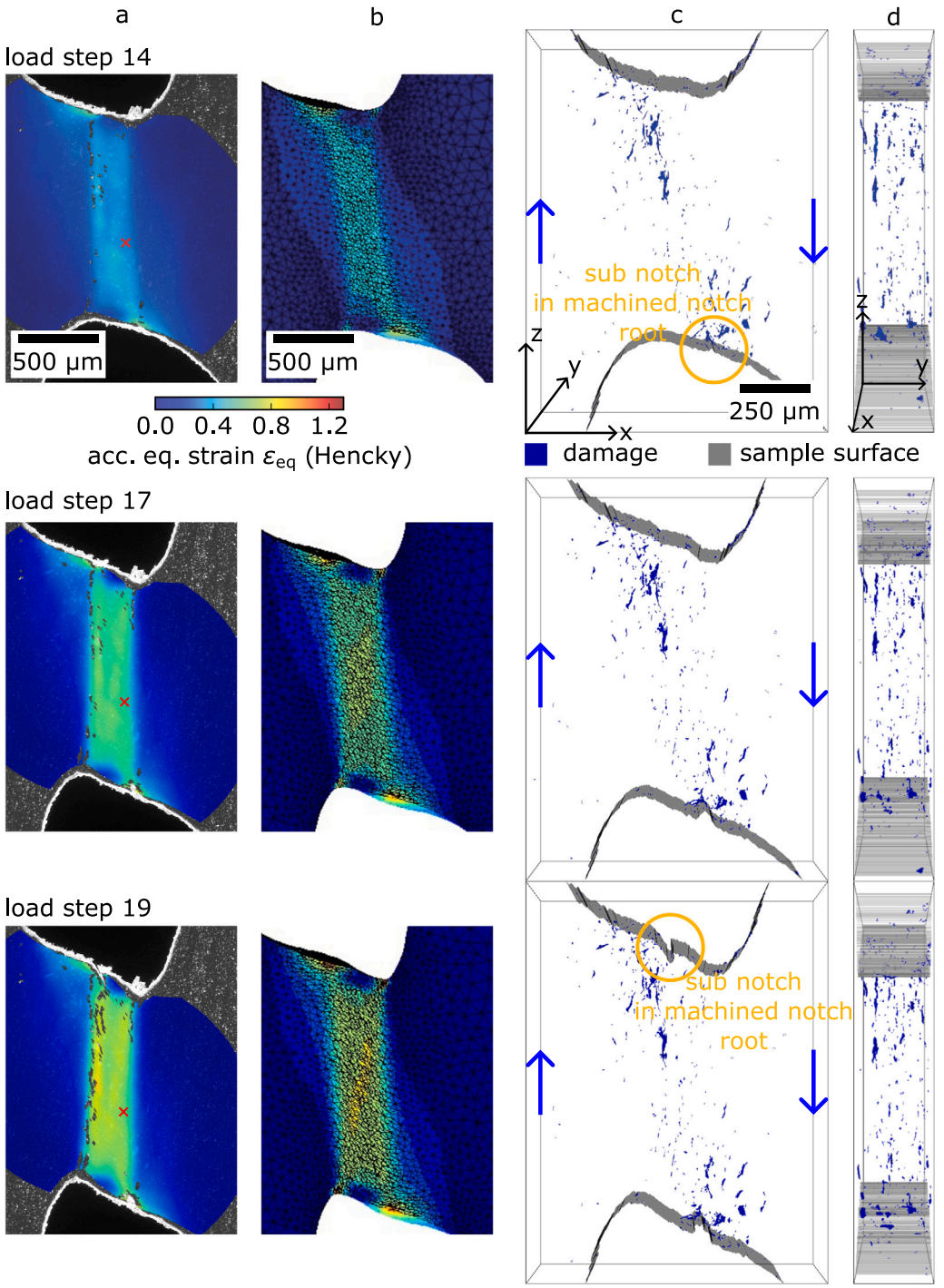

Fig. 6. Mesoscale developments during shear loading (after tension). (a) measured and (b) simulated acc. eq. Hencky strain in the sample center. 3D renderings of the corresponding damage features (c) normal to the sheet plane, (d) normal to the fracture plane.

step 8, with an approximate size of 100 µm in the z direction, a few µm in the x direction and a few tens of µm in the y direction. The volume of the damage feature is quantified relatively to its size after tension loading in Fig. 10(c). Similar to the average development of larger damage features, the detrimental feature grows exponentially during tension and linearly under shear. The volume of the detrimental feature increases by 96 % under shear, and the feature is strongly elongated along the z direction (loading

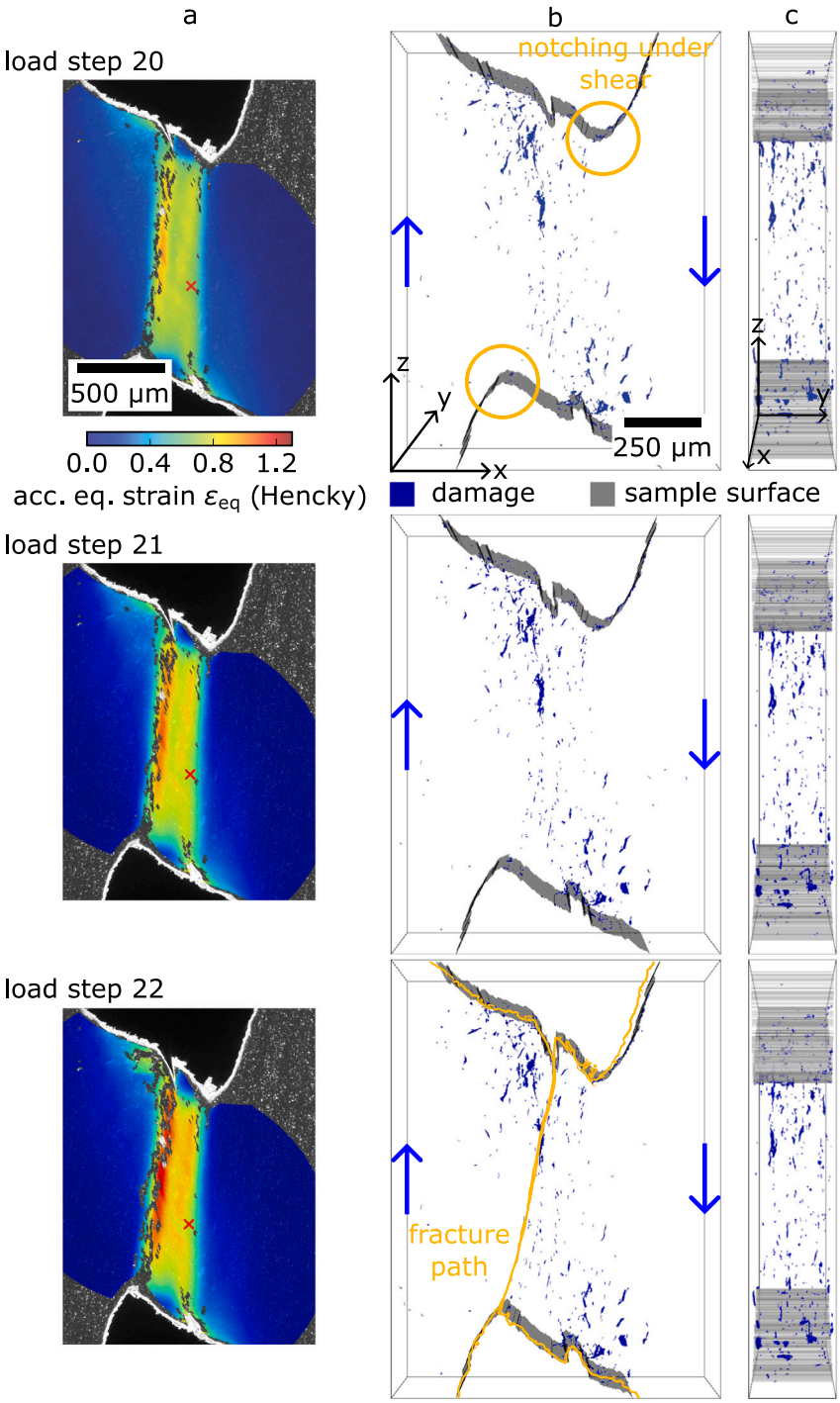

Fig. 7. Mesoscale developments during final shear loading (after tension). (a) measured acc. eq. Hencky strain in the sample center. 3D renderings of the corresponding damage features, (c) normal to the sheet plane, (d) normal to the fracture plane.

direction) up to a length of approximately 300 µm. Furthermore, the detrimental damage feature coincides with the sub shear band having the highest acc. eq. strain (Figs. 7 and 8).

3.3. Microscale observations

The above described mesoscale study of strain and grain-related damage enables the selection of representative ROIs for the study of particle-induced shear damage mechanisms. Due to the typical sizes of a few µm, which are close to the resolution limit

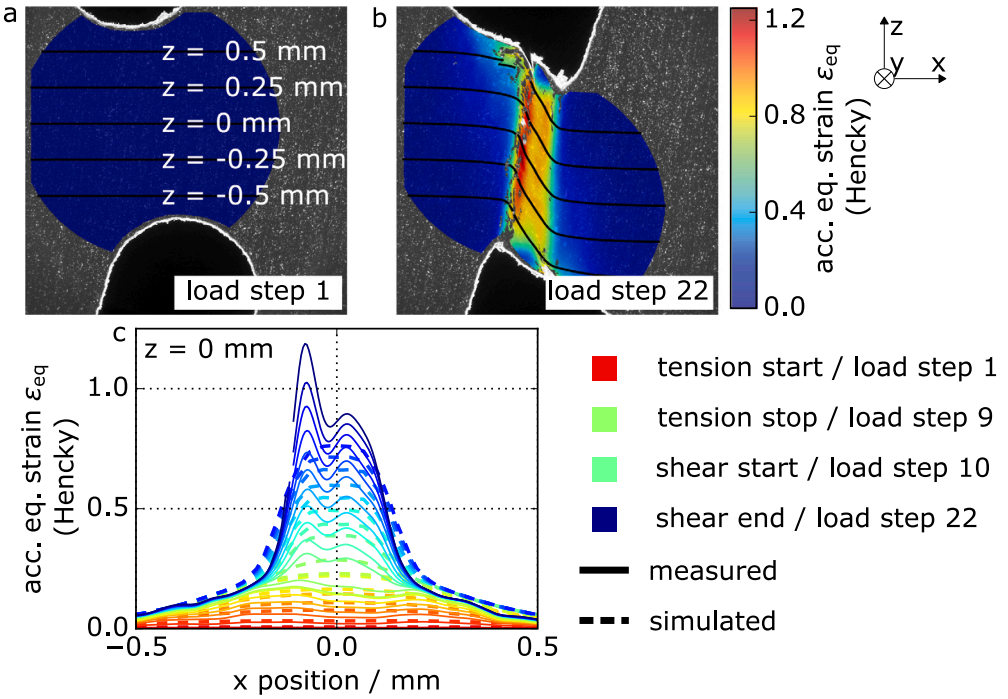

Fig. 8. Mesoscale deformation: (a) and (b) display the P-DIC based Hencky strain maps in the deformed and undeformed states. (c) shows the measured accumulated equivalent strain along the line profile $L = 0\,\text{mm}$ (indicated in (a)) for different load steps. The dashed curves represent simulated accumulated equivalent strain along the corresponding profile line. Two prominent peaks are observed in the measured strain profile. Measured strain along lines $L \neq 0\,\text{mm}$ can be found in the supplements.

of the CL measurements, only a few damage intermetallic particle cluster are analyzed (manual segmentation is necessary). The 3D spatial resolution is about 2 µm to 3 µm. Smaller features like inclusions or cracks in intermetallic particles or the aluminum matrix are barely distinguishable. Based on the mesoscale analysis, the investigated ROI is selected such that it lies well within the observed shear band and is as far as possible from the accumulation of grain-related damage features.

Fig. 11(a) displays the central slices of the cluster under investigation for selected load steps. The location of the selected ROI is indicated in Figs. 5–7 by a red cross. Fig. 11(b) illustrates the manual segmentation of the entire cluster. Corresponding slices and segmented volumes for all load steps are available in the supplementary materials. Fig. 11(c) quantifies the growth of the damage features illustrated in (b). It is observed that the damage nucleates at load step 7 (acc. eq. strain $\varepsilon_{eq} = 0.3$) due to intermetallic particle fracture. Unlike the exponential growth observed for grain-related damage features, damage growth during tension is linear. Under shear loading, the observed damage feature exhibits a strong, linear growth of 655 %. The maximum relative void volume is reached at the forelast loading step, during the last measured step before fracture the relative void volume drops to 546 %. As indicated in Fig. 11(a), the sub cluster marked in orange appears to undergo rotation. This rotation is quantified in Fig. 11(d), showing an approximate rotation from 26° to 66°. Particularly, during tension, the measured angle fluctuates, attributed to the round particle shape, making it impossible to determine precise rotation angles. The quantified effective rotation of the cluster, mainly results from a translation of different cluster fragments and the formation of voids.

To validate and understand the experimentally observed shear-driven particle-related void growth, three-dimensional FEM of the observed and an idealized particle-void cluster were performed. The clusters are meshed at load step 9 using a volumetric mesh including voids and intermetallic particles. An elastic modulus of $E = 70\,\text{GPa}$ was assumed for the aluminum matrix, while intermetallic particles were modeled with an increased elastic modulus of $E = 235\,\text{GPa}$ (Zhang et al., 2021). This configuration is referred to as elastic particles. An additional simulation scenario represents the absence of intermetallic particles by assigning them the same elasto-plastic behavior as the aluminum matrix. This case is referred to as no particles. The corresponding meshes for the idealized and measured particle-void cluster are shown for representative load steps in Fig. 12(a) and (b). The idealized void cluster provides a schematic of particle-induced damage growth under shear. The mesh shown in Fig. 12(b) corresponds to the particle-void cluster studied in Fig. 11. A mesh sensitivity analysis was conducted for both idealized and measured particle-void clusters. Results shown here are independent of the chosen mesh size.

Displacement vectors are extracted from mesoscale DIC measurements (in-plane components only; for reference see Figs. 6 and 7). These DIC-based measured boundary conditions are applied to the FE simulation, of the microscale particle-void clusters. The measured boundary conditions exhibit strong shear components U_{zx} and U_{xz}, as well as finite normal components U_{xx} and U_{zz} (see Fig. 12(c) and (d)). Although the stretch tensor therefore appears triaxial, the non-zero in-plane normal components

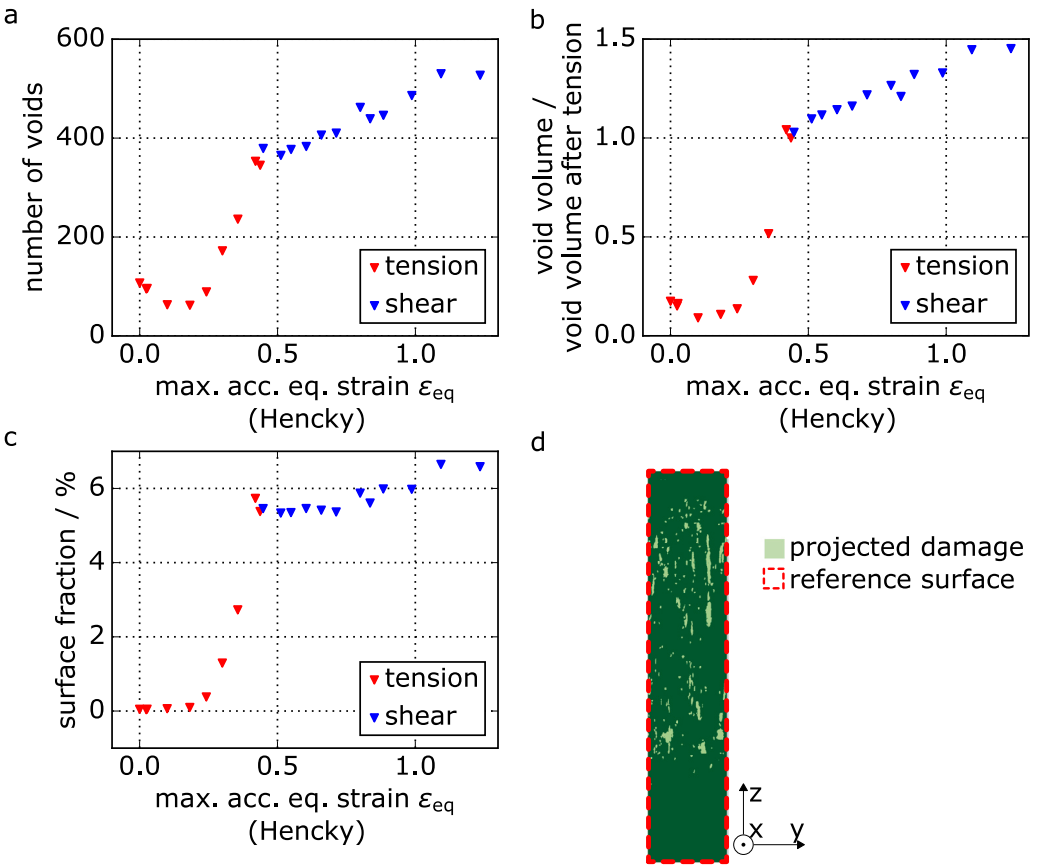

Fig. 9. Mesoscale damage quantification: Statistical analysis of the development of grain-related damage. In the shown statistics, only features with void volumes $\geq(4.45\,\mu m)^3$ are considered. (a) number of voids as a function of maximum accumulated eq. strain. (b) corresponding normalized void volume. (c) surface fraction of the projected damage along the x axis. (d) reference surface used to determine the damage surface fraction.

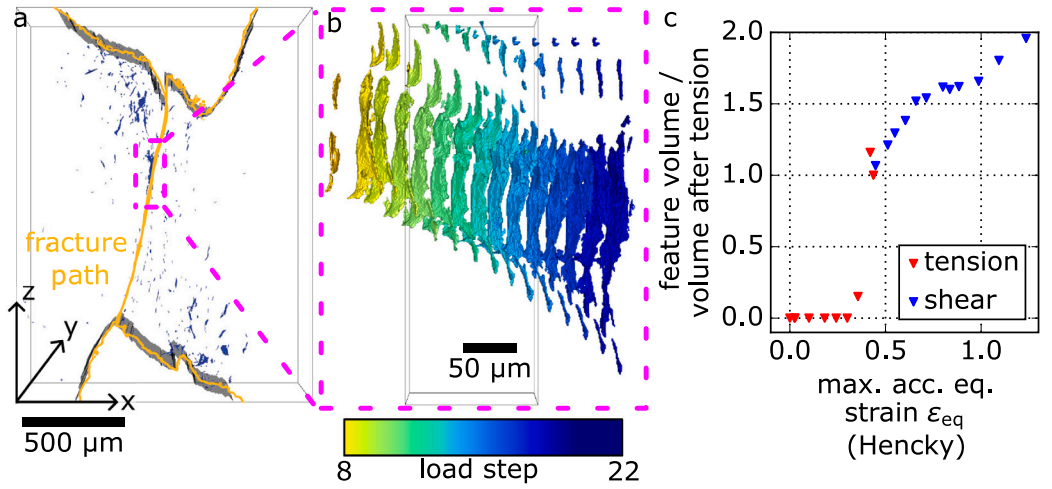

Fig. 10. Correlation of micro and mesoscale observations. (a) damage field, sample surface, and fracture path. (b) zoom-in on the detrimental feature, displaying its development. (c) quantification of the development of the detrimental feature. Initiated under tension (load step 8), the detrimental feature grows subsequently during the shear phase (see (b) and (c)). Its position coincidences with the strong strain localization visible in Fig. 8 and the final fracture path.

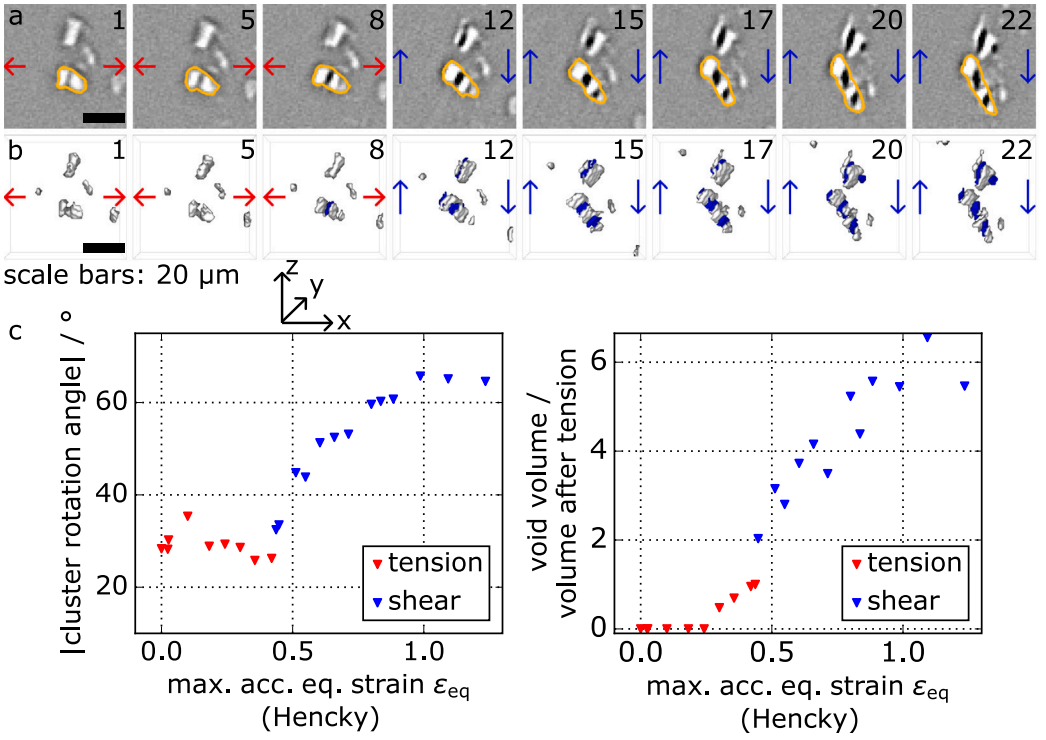

Fig. 11. Particle-induced void growth under shear by *in situ* CL. (a) central laminographic slice, showing the cluster development for different load steps. (b) volume rendering of the cluster development for different load steps. (c) quantification of the void volume growth as a function of maximum accumulated equivalent strain. (d) angular development of the intermetallic particle and particle-void cluster highlighted in (a). The rotation of the cluster does not correspond to a rotation of intermetallic particles, but rather to a fracture of the particle and subsequent relative translation of the different particle fragments.

($U_{xx}-1$ and $U_{zz}-1$) are not associated with externally imposed tensile loading. Instead, they originate from the large shear component through the polar decomposition of the deformation gradient, which leads to a rotation of the principal stretches with respect to the coordinate axes. The apparent triaxiality is thus shear-induced, and the observed void growth can be classified as shear-driven. In addition to the DIC-based boundary conditions, idealized simple shear conditions were also considered. In this case, only the displacement components in the z-direction was prescribed, while all displacement components in the x-direction were constrained to zero. Similarly to the DIC-based boundary conditions, idealized simple shear also leads to evolving tensile stretch components. In fact, for a simple shear deformation gradient of the form $\boldsymbol{F} = \mathbf{1} - \gamma \boldsymbol{e}_3 \otimes \boldsymbol{e}_1 = \boldsymbol{R} \cdot \boldsymbol{U}$, the rotation and stretch tensors take the following expressions (Forest, 2022):

$$\boldsymbol{R} = \begin{bmatrix} \frac{1}{\sqrt{1+(\gamma/2)^2}} & 0 & \frac{\gamma}{2\sqrt{1+(\gamma/2)^2}} \\ 0 & 1 & 0 \\ \frac{-\gamma}{2\sqrt{1+(\gamma/2)^2}} & 0 & \frac{1}{\sqrt{1+(\gamma/2)^2}} \end{bmatrix}, \tag{3}$$

$$\boldsymbol{U} = \begin{bmatrix} \frac{1+\gamma^2/2}{\sqrt{1+(\gamma/2)^2}} & 0 & \frac{-\gamma}{2\sqrt{1+(\gamma/2)^2}} \\ 0 & 1 & 0 \\ \frac{-\gamma}{2\sqrt{1+(\gamma/2)^2}} & 0 & \frac{1}{\sqrt{1+(\gamma/2)^2}} \end{bmatrix}. \tag{4}$$

For all investigated cases, shear-driven void growth is observed. In the idealized particle-void cluster (see Fig. 12(d)), measured boundary conditions lead to a relative void growth of up to a factor of six, whereas idealized simple shear boundary conditions result in a reduced maximum void growth of approximately 3.5. When intermetallic particles are neglected, only minor void growth of about 2.5 is observed. For the measured particle-void cluster (see Fig. 12(e)), the overall void growth is smaller: elastic particles under measured boundary conditions show void growth exceeding a factor of three, simulations of elastic particles under idealized simple shear boundary conditions results in void growth slightly above 2.5, and the no particle case exhibits the smallest growth of approximately 1.5.

Overall, the simulations show that increasing initial void volume fraction leads to reduced relative void growth rates.

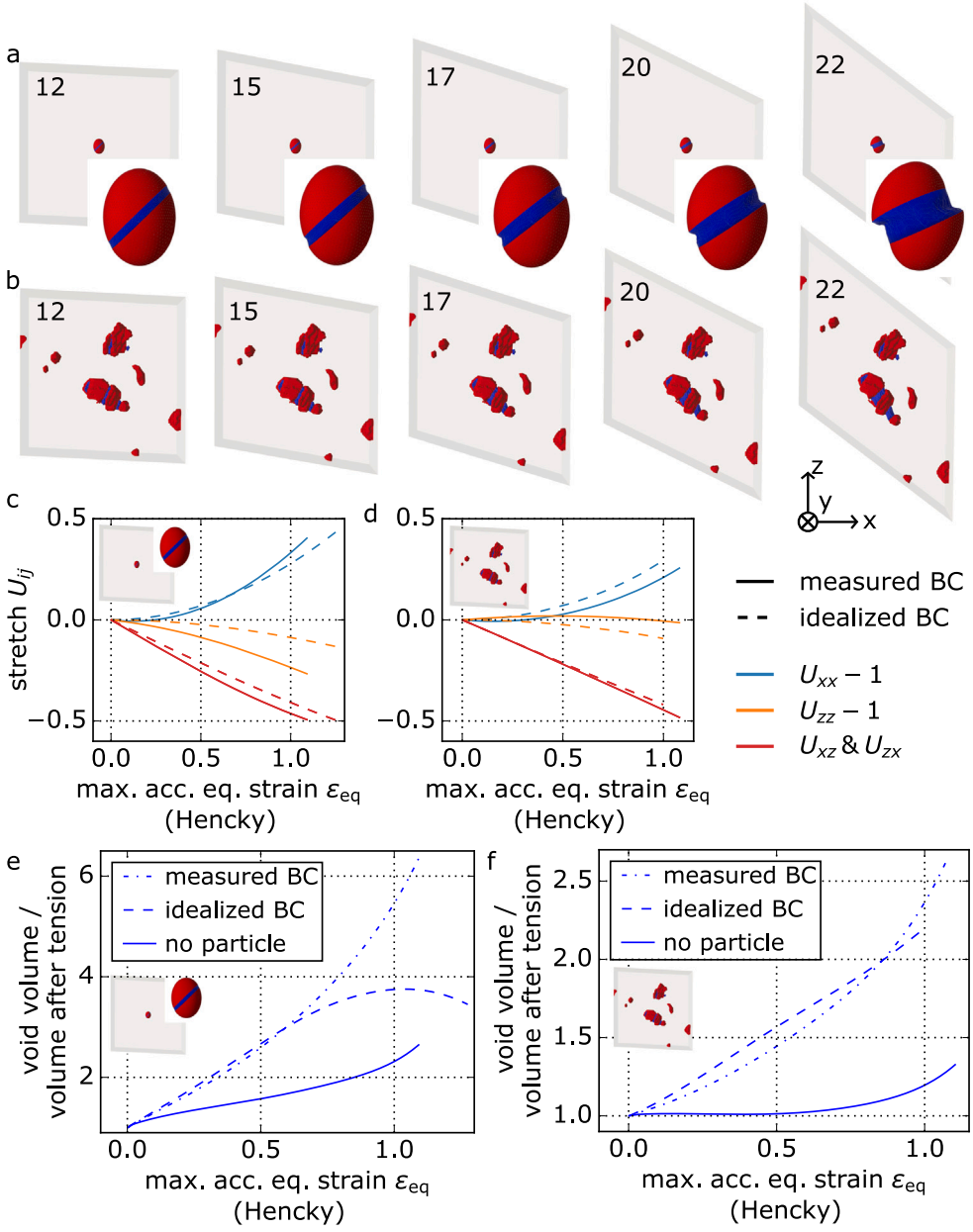

Fig. 12. Particle-induced shear-driven void growth by micromechanical FEM simulations. Evolving mesh of the simulated simplified particle-void cluster (a) and the measured particle-void cluster (b). Measured and idealized simple shear boundary conditions applied for the simplified (c) and measured (d) void cluster. Simulated void growths for the simplified (e) and measured particle-void cluster (f).

4. Discussion

In the previous section, damage nucleation and development during a 'tension to shear' load path change experiment is observed. Specifically, the study focuses on inducing damage under tension and then monitoring and quantifying the damage evolution under shear. A hierarchical approach is employed to approach the question of particle related void growth under shear. On the macro- and mesoscale strain fields and large grain related damage features are carefully studied to extract a ROI allowing the study of microscale phenomena under shear. The microscale ROI is selected such that the observed particle-void cluster is located within the shear band and well separated from larger grain related damage.

This allows a thorough study of intermetallic-related damage. This type of damage is qualitatively described by literature (Buljac et al., 2023; Tancogne-Dejean et al., 2021). In this study, we quantified the growth of intermetallic-related damage, and found a

remarkable growth of 655 % volume increase during shear. This growth mechanisms can be explained by void-locking (Tvergaard, 2011), where the interaction of a ductile aluminum matrix with stiff particles leads to a volume growth. Here it is found, that a particle cluster fractures, and the fragments are translated under shear, leading to an effective rotation of the cluster. The translation further opens the damage features. A void growth factor of up to six under shear is validated by volumetric FEM. The simulation results vary, predicting relative void growth factors between approximately 2.5 and 6. This variability arises from the strong sensitivity of the simulations to the applied boundary conditions, the initial void volume fraction, as well as the intrinsic measurement uncertainties associated with these parameters. For all simulated cases in the absence of intermetallic particles, void growth is strongly suppressed, underscoring the crucial role of intermetallic particles in promoting void growth. For the last loading step, a decreased relative void volume is observed in the measured data. At first glance, this might be attributed to measurement uncertainty. However, Tancogne-Dejean et al. (2021) reported a reduction in void numbers towards the end of a shear loading test, which they attributed to the closure of voids, such that they cannot be resolved anymore. Additionally, simulations of an idealized void under idealized simple shear boundary conditions indicate that this drop might be a real physical effect. Due to the small scale of the damage feature, only a single feature is analyzed. To reduce the above-mentioned measurement uncertainties future nanoscale *in situ* laminography observations (Hurst et al., 2023) would be beneficial. Further such measurements would allow for an automated data segmentation and thus statistical analysis for particle related damage mechanisms.

The pre-characterization on meso- and macroscale, necessary to determine a representative ROI for the study of particle induced damage revealed additional findings: Based on the size and morphology of the larger damage features, it is concluded that they are linked to the grain structure of the material. In Kong et al. (2024), this conclusion is supported by scanning electron microscopy and electron backscatter microscopy analyses of an arrested shear loaded AA2198-T851 specimen.

For the studied specimen it is evident that these grain-related damage features are key for the specimen's final failure. They induce inhomogeneity in the expected shear, creating sub shear bands on the mesoscale. This dissipation of energy in different shear bands (i.e., in the band from shear notch to shear notch and in the band from sub notch in the machined notch root to a shear notch) may explain the increased macroscopic ductility in terms of stretch to fracture. While the nucleation and growth of such damage features under high stress triaxiality are expected and can be captured by existing models (Gurson, 1977; Tvergaard and Needleman, 1984), this study enables us to observe and quantify the development of grain-related damage under shear load at zero stress triaxiality. A linear volume increase of 45 % during shear is quantified, the underlying mechanisms for the increase of the grain-related damage remain unknown. In Kong et al. (2024), based on an electron backscatter diffraction study, we found indications, suggesting that such damage features are either trans- or intergranular, necessitating different descriptions by distinct growth models. A deeper understanding of the origin of these damage features could be gained by X-ray diffraction methods (Gille et al., 2024; Herbig et al., 2011; Yildirim et al., 2023).

5. Conclusions

A 'tension to shear' load path change experiment on a AA2198-T851 sheet specimen has been designed to study the evolution of damage features under shear which nucleated under tension. The deformation and damage is observed and quantified on multiple scales using 3D in situ computed laminography and correlative surface imaging. This multiscale approach allows a detailed study of strain conditions and morphological behavior of particle-induced damage growth under shear by void locking. To enable quantification and modeling of the void locking effect, strain conditions and damage fields are carefully characterized and validated by simulations on the macro- and mesoscale. This allows the study of void locking by morphological analysis and detailed FEM simulations.

The key findings are: Experimental and theoretical evidence for particle-induced shear damage growth.

- *In situ* laminography measurements show that intermetallic-related damage nucleates under tension and grows further during shear. A remarkable volume increase during shear is quantified for a representative particle-void cluster. The measured volume increase is 655 %.
- Particle-induced shear growth is studied by micromechanical FEM simulations, validating particle-induced void growth under shear. The simulations show a high sensitivity to the initial void volume and the applied boundary conditions. The simulated particle-induced void growth ranges from 600 % to 250 %.
- We attribute the observed particle-induced void growth under shear to a void locking mechanism.
- This is supported by micromechanical simulations without particles, in which pre-existing voids showed a much smaller growth rate.

In addtion to the particle-related findings the necessary pre investigation revealed insights to macro- and mesoscale damage mechanisms:

On the macroscale we observe an increased stretch to fracture and decreased nominal maximum stress for the load path change experiment compared to monotonic shear-only loading.

On the mesoscale we find similar average strain levels in experiment and simulation. But during shear, the measured strain shows two peaks at the border of the shear band, which is not predicted by the simulation. The inhomogeneity is caused by grain-related damage features nucleated during tension. Further grain-related damage nucleation and exponential growth versus equivalent strain is found under tension (under high stress triaxiality), followed by moderate and linear growth under shear (under low stress triaxiality), quantified and correlated to strain for a statistical relevant number of damage features. The total damage

volume of grain-related damage grew by 45 % during shear. The damage volume of the grain-related, detrimental feature grew by 96 %. This detrimental feature coincidences with the fracture path. The nucleation and growth under shear of these grain-related damage features cannot be explained by classical void growth models. Sub notches in the machined notch root during shear phase under non-zero stress triaxiality are found, further shear notches under zero stress triaxiality are forming. The final failure from a shear notch to a sub notch in the machined notch root is observed and driven by an intergranular damage feature.

Summarizing, competing fracture mechanisms have been found, quantified and discussed. The most notable finding is the experimental evidence for the void-locking mechanism, which is further validated by micromechanical FEM simulations. The observed grain-related damage features cannot be explained by existing models. Motivating complementary measurements of grain- and microsturcture by *in situ* CL and crystal-plasticity simulations.

CRediT authorship contribution statement

Mathias Hurst: Writing – original draft, Visualization, Software, Methodology, Investigation, Formal analysis, Data curation, Conceptualization. **Jean-Michel Scherer:** Visualization, Software, Methodology, Formal analysis. **Xiang Kong:** Writing – review & editing, Visualization, Software, Formal analysis. **Maryse Gille:** Methodology, Investigation. **Simon Bode:** Methodology, Investigation. **Djamel Missoum-Benziane:** Methodology, Investigation. **Tilo Baumbach:** Writing – review & editing, Funding acquisition. **Lukas Helfen:** Writing – review & editing, Methodology, Investigation, Funding acquisition, Conceptualization. **Thilo F. Morgeneyer:** Writing – original draft, Resources, Methodology, Investigation, Funding acquisition, Conceptualization.

Declaration of competing interest

The authors declare that they have no known competing financial interests or personal relationships that could have appeared to influence the work reported in this paper.

Acknowledgments

The work is funded by the Deutsche Forschungsgemeinschaft (DFG, German Research Foundation) – 391911929/02012170081 and the French National Research Agency (ANR-17-CE08-0051) within their joint research project LAMBDA. Mathias Hurst received funding from the 'InnovationsCampus Mobilität der Zukunft'. We acknowledge the European Synchrotron Radiation Facility (ESRF) for provision of synchrotron radiation facilities under proposal number blc13800, and we would like to thank Marta Majkut and Ludovic Broche for assistance and support in using beam line ID19.

We acknowledge the KIT Light Source for provision of the Lamino-II station at the IMAGE beam line, and we would like to thank the Institute for Beam Physics and Technology (IBPT) for the operation of the storage ring, the Karlsruhe Research Accelerator (KARA).

Daniel Hänschke is acknowledged for supporting discussions, and Gabriel Lefloch is acknowledged for language revision. *Constellium Technology Center (C-TEC), Voreppe, France* is acknowledged for materials supply.

Appendix A. Supplementary data

Supplementary material related to this article can be found online at https://doi.org/10.1016/j.ijplas.2026.104724.

Data availability

Data will be made available on request.

References

Abedini, A., Butcher, C., Worswick, M., 2018. Experimental fracture characterisation of an anisotropic magnesium alloy sheet in proportional and non-proportional loading conditions. Int. J. Solids Struct. 144–145, 1–19.

Achouri, M., Germain, G., Dal Santo, P., Saidane, D., 2013. Experimental characterization and numerical modeling of micromechanical damage under different stress states. Mater. Des. 50, 207–222.

Azman, M., Le Bourlot, C., King, A., Fabrègue, D., Maire, E., 2022. 4D characterisation of void nucleation, void growth and void coalescence using advanced void tracking algorithm on in situ X-ray tomographic data. Mater. Today Commun. 32, 103892.

Babout, L., Brechet, Y., Maire, E., Fougères, R., 2004. On the competition between particle fracture and particle decohesion in metal matrix composites. Acta Mater. 52 (15), 4517–4525.

Bao, Y., Wierzbicki, T., 2004. On fracture locus in the equivalent strain and stress triaxiality space. Int. J. Mech. Sci. 46 (1), 81–98.

Besson, J., Foerch, R., 1997. Large scale object-oriented finite element code design. Comput. Methods Appl. Mech. Engrg. 142 (1), 165–187.

Bron, F., Besson, J., 2004. A yield function for anisotropic materials application to aluminum alloys. Int. J. Plast. 20 (4–5), 937–963.

Brünig, M., Zistl, M., Gerke, S., 2021. Numerical analysis of experiments on damage and fracture behavior of differently preloaded aluminum alloy specimens. Metals 11, 381.

Buljac, A., Kong, X., Helfen, L., Hild, F., Morgeneyer, T.F., 2023. Shear loading dominated damage mechanisms and strain localization studied by in situ 3D laminography imaging and digital volume correlation for AA2198-T8. Mech. Mater. 178, 104558.

Cecilia, A., Simon, R., Hamann, E., Zuber, M., Faragó, T., Hänschke, D., Hurst, M., van de Kamp, T., Bauer, S., Spiecker, R., Czyzycki, M., Gasilov, S., Ershov, A., Reszat, J.-T., Baumbach, T., 2025. The IMAGE beamline at the KIT light source. J. Synchrotron Radiat. 32 (4), 1036–1051.

Croom, B.P., Jin, H., Noell, P.J., Boyce, B.L., Li, X., 2019. Collaborative ductile rupture mechanisms of high-purity copper identified by in situ X-ray computed tomography. Acta Mater. 181, 377–384.

Faragó, T., Gasilov, S., Emslie, I., Zuber, M., Helfen, L., Vogelgesang, M., Baumbach, T., 2022. *Tofu*: a fast, versatile and user-friendly image processing toolkit for computed tomography. J. Synchrotron Radiat. 29 (3), 916–927.

Fleck, N., Hutchinson, J., Tvergaard, V., 1989. Softening by void nucleation and growth in tension and shear. J. Mech. Phys. Solids 37, 515–540.

Forest, S., 2022. Mécanique des milieux continus. volume 1: théorie. Presses des Mines.

Gille, M., Proudhon, H., Oddershede, J., Quey, R., Morgeneyer, T.F., 2024. 3D strain heterogeneity and fracture studied by X-ray tomography and crystal plasticity in an aluminium alloy. Int. J. Plast. 104146.

Gologanu, M., Leblond, J.-B., Perrin, G., Devaux, J., 1997. Recent extensions of Gurson's model for porous ductile metals. In: Continuum Micromechanics. Springer, pp. 61–130.

Gross, A.J., Ravi-Chandar, K., 2016. On the deformation and failure of Al 6061-T6 at low triaxiality evaluated through in situ microscopy. Int. J. Fract. 200, 185–208.

Gurson, A.L., 1977. Continuum theory of ductile rupture by void nucleation and growth: Part I—Yield criteria and flow rules for porous ductile media. J. Eng. Mater. Technol. 99 (1), 2–15.

Han, G., He, J., Li, S., Lin, Z., 2024. Simple shear methodology for local structure–property relationships of sheet metals: State-of-the-art and open issues. Prog. Mater. Sci. 143, 101266.

Hannard, F., Pardoen, T., Maire, E., Le Bourlot, C., Mokso, R., Simar, A., 2016. Characterization and micromechanical modelling of microstructural heterogeneity effects on ductile fracture of 6xxx aluminium alloys. Acta Mater. 103, 558–572.

Hannard, F., Simar, A., Maire, E., Pardoen, T., 2018. Quantitative assessment of the impact of second phase particle arrangement on damage and fracture anisotropy. Acta Mater. 148, 456–466.

Helfen, L., Baumbach, T., Mikulík, P., Kiel, D., Pernot, P., Cloetens, P., Baruchel, J., 2005. High-resolution three-dimensional imaging of flat objects by synchrotron-radiation computed laminography. Appl. Phys. Lett. 86 (7), 071915.

Herbig, M., King, A., Reischig, P., Proudhon, H., Lauridsen, E., Marrow, T., Buffiere, J.-Y., Ludwig, W., 2011. 3D growth of a short fatigue crack within a polycrystalline microstructure studied using combined diffraction and phase-contrast X-ray tomography. Acta Mater. 59, 590–601.

Hurst, M., 2024. Methodology for 4D X-ray Microscopy and Its Application in Material Science (Ph.D. thesis). Karlsruhe Institute of Technology, pp. 73–75.

Hurst, M., Helfen, L., Morgeneyer, T.F., Suhonen, H., Buljac, A., Hild, F., Suuronen, J.-P., Baumbach, T., Hänschke, D., 2023. Hierarchically guided in situ nanolaminography for the visualisation of damage nucleation in alloy sheets. Sci. Rep. 13 (1), 1055.

Kanopoulos, N., Vasanthavada, N., Baker, R.L., 1988. Design of an image edge detection filter using the Sobel operator. IEEE J. Solid-State Circuits 23 (2), 358–367.

Kong, X., Chen, J., Madi, Y., Missoum-Benziane, D., Besson, J., Morgeneyer, T., 2023. Plasticity and ductility of an anisotropic recrystallized AA2198 Al-Cu-Li alloy in T3 and T8 conditions during proportional and non-proportional loading paths: simulations and experiments. J. Theor. Comput. Appl. Mech..

Kong, X., Helfen, L., Hurst, M., Hänschke, D., Missoum-Benziane, D., Besson, J., Baumbach, T., Morgeneyer, T.F., 2022. 3D in situ study of damage during a 'shear to tension' load path change in an aluminium alloy. Acta Mater. 117842.

Kong, X., Hurst, M., Helfen, L., Gaslain, F., Baumbach, T., Suhonen, H., Morgeneyer, T., 2024. Ductile shear damage micromechanisms studied by correlative multiscale nanotomography and SEM/EBSD for a recrystallized aluminum alloy 2198 T8. J. Mater. Sci. 59, 13690–13708.

Kuna, M., Sun, D.-Z., 1996. Analyses of void growth and coalescence in cast iron by cell models. Le J. Phys. IV 6 (C6), C6–113.

Landron, C., Bouaziz, O., Maire, E., Adrien, J., 2010. Characterization and modeling of void nucleation by interface decohesion in dual phase steels. Scr. Mater. 63 (10), 973–976.

Landron, C., Maire, E., Adrien, J., Bouaziz, O., Di Michiel, M., Cloetens, P., Suhonen, H., 2012. Resolution effect on the study of ductile damage using synchrotron X-ray tomography. Nucl. Instrum. Methods Phys. Res. Sect. B 284, 15–18.

Landron, C., Maire, E., Bouaziz, O., Adrien, J., Lecarme, L., Bareggi, A., 2011. Validation of void growth models using X-ray microtomography characterization of damage in dual phase steels. Acta Mater. 59 (20), 7564–7573.

Lecarme, L., Maire, E., Kumar K.C., A., De Vleeschouwer, C., Jacques, L., Simar, A., Pardoen, T., 2014. Heterogenous void growth revealed by in situ 3-D X-ray microtomography using automatic cavity tracking. Acta Mater. 63, 130–139.

Madi, Y., Garcia, J.-M., Proudhon, H., Shinohara, Y., Helfen, L., Besson, J., Morgeneyer, T.F., 2019. On the origin of the anisotropic damage of X100 line pipe steel: Part I - In situ synchrotron tomography experiments. Integr. Mater. Manuf. Innov. 8, 570–596.

Maire, E., Withers, P.J., 2014. Quantitative X-ray tomography. Int. Mater. Rev. 59 (1), 1–43.

Maire, E., Zhou, S., Adrien, J., Dimichiel, M., 2011. Damage quantification in aluminium alloys using in situ tensile tests in X-ray tomography. Eng. Fract. Mech. 78 (15), 2679–2690.

Morgeneyer, T.F., Khadyko, M., Buljac, A., Helfen, L., Hild, F., Benallal, A., Børvik, T., Hopperstad, O.S., 2021. On crystallographic aspects of heterogeneous plastic flow during ductile tearing: 3D measurements and crystal plasticity simulations for AA7075-T651. Int. J. Plast. 144, 103028.

Morgeneyer, T.F., Taillandier-Thomas, T., Helfen, L., Baumbach, T., Sinclair, I., Roux, S., Hild, F., 2014. In situ 3-D observation of early strain localization during failure of thin Al alloy (2198) sheet. Acta Mater. 69, 78–91.

Myagotin, A., Voropaev, A., Helfen, L., Hänschke, D., Baumbach, T., 2013. Efficient volume reconstruction for parallel-beam computed laminography by filtered backprojection on multi-core clusters. IEEE Trans. Image Process. 22, 5348–5361.

Nahshon, K., Hutchinson, J., 2008. Modification of the Gurson model for shear failure. Eur. J. Mech. A Solids 27 (1), 1–17.

Nielsen, K.L., Dahl, J., Tvergaard, V., 2012. Collapse and coalescence of spherical voids subject to intense shearing: studied in full 3D. Int. J. Fract. 177, 97–108.

Papasidero, J., Doquet, V., Mohr, D., 2015. Ductile fracture of aluminum 2024-T351 under proportional and non-proportional multi-axial loading: Bao–Wierzbicki results revisited. Int. J. Solids Struct. 69–70, 459–474.

Pineau, A., Benzerga, A., Pardoen, T., 2016. Failure of metals I: Brittle and ductile fracture. Acta Mater. 107, 424–483.

Ren, S.C., Morgeneyer, T.F., Mazière, M., Forest, S., Rousselier, G., 2019. Portevin-Le Chatelier effect triggered by complex loading paths in an Al–Cu aluminium alloy. Phil. Mag. 99 (6), 659–678.

Roth, C.C., Mohr, D., 2016. Ductile fracture experiments with locally proportional loading histories. Int. J. Plast. 79, 328–354.

Roth, C.C., Mohr, D., 2018. Determining the strain to fracture for simple shear for a wide range of sheet metals. Int. J. Mech. Sci. 149, 224–240.

Siruguet, K., Leblond, J.-B., 2004. Effect of void locking by inclusions upon the plastic behavior of porous ductile solids—I: theoretical modeling and numerical study of void growth. Int. J. Plast. 20 (2), 225–254.

Tancogne-Dejean, T., Roth, C.C., Morgeneyer, T.F., Helfen, L., Mohr, D., 2021. Ductile damage of AA2024-T3 under shear loading: Mechanism analysis through in-situ laminography. Acta Mater. 205, 116556.

Toda, H., Takijiri, A., Azuma, M., Yabu, S., Hayashi, K., Seo, D., Kobayashi, M., Hirayama, K., Takeuchi, A., Uesugi, K., 2017. Damage micromechanisms in dual-phase steel investigated with combined phase- and absorption-contrast tomography. Acta Mater. 126, 401–412.
Torki, M.E., Benzerga, A.A., 2018. A mechanism of failure in shear bands. Extrem. Mech. Lett. 23, 67–71.
Tvergaard, V., 2008. Shear deformation of voids with contact modelled by internal pressure. Int. J. Mech. Sci. 50, 1459–1465.
Tvergaard, V., 2009. Behaviour of voids in a shear field. Int. J. Fract. 158, 41–49.
Tvergaard, V., 2011. Void shape effects and voids starting from cracked inclusion. Int. J. Solids Struct. 48 (7), 1101–1108.
Tvergaard, V., Needleman, A., 1984. Analysis of the cup-cone fracture in a round tensile bar. Acta Metall. 32 (1), 157–169.
Wei, Z., Gerke, S., Brünig, M., 2024. Ductile damage and fracture characterizations in bi-cyclic biaxial experiments. Int. J. Mech. Sci. 276, 109380.
Wu, S., Xiao, T., Withers, P., 2017. The imaging of failure in structural materials by synchrotron radiation X-ray microtomography. Eng. Fract. Mech. 182, 127–156.
Yildirim, C., Poulsen, H., Winther, G., Detlefs, C., Huang, P., Dresselhaus-Marais, L., 2023. Extensive 3D mapping of dislocation structures in bulk aluminum. Sci. Rep. 13, 3834.
Zhang, X., Wang, D., Zhou, Y., Chong, X., Li, X., Zhang, H., Nagaumi, H., 2021. Exploring crystal structures, stability and mechanical properties of Fe, Mn-containing intermetallics in Al-Si alloy by experiments and first-principles calculations. J. Alloys Compd. 876, 160022.